Chemical Science

ROYAL SOCIETY OF CHEMISTRY

EDGE ARTICLE

View Article Online
View Journal

Open Access Article. Published on 23 January 2026. Downloaded on 3/17/2026 3:33:40 PM.
This article is licensed under a Creative Commons Attribution-NonCommercial 3.0 Unported Licence.

Check for updates

Cite this: DOI: 10.1039/d5sc08236f

All publication charges for this article have been paid for by the Royal Society of Chemistry

Received 24th October 2025
Accepted 22nd January 2026

DOI: 10.1039/d5sc08236f

rsc.li/chemical-science

Electrostatic decatalysis through coulombic screening

Bhojkumar Nayak,[a] Abdul Raafik Arattu Thodika,[b] Hemanga Pradhan,[a] Rahul Mahadeo Mendhe[a] and Musthafa Ottakam Thotiyl *[a]

We demonstrate electrostatic decatalysis, where long-range coulombic interactions selectively screen parasitic chemistry, leading to distinct catalytic selectivity outcomes. By reconfiguring interfacial electrostatic landscapes, this approach achieves site- and flux-selective modulation of competing reactions while promoting ammonia electrosynthesis. Molecular dynamics simulations reveal a nearly sevenfold enhancement in substrate enrichment factors, arising from optimized electrostatic screening and strategic charge distribution. Experimentally, we observe more than a twofold increase in ammonia's faradaic efficiency at practically relevant current densities, suggesting electrostatics contribute to reaction selectivity with energy savings exceeding 50% relative to conventional benchmarks. Importantly, this approach based on activation of coulombic forces exhibits pH-insensitive universality, enabling broad applicability for electrochemical process modulations.

Introduction

Electrocatalysis is at the heart of transformative technologies spanning energy storage, green synthesis, and environmental remediation.[1–7] Yet, achieving high activity and selectivity for challenging reactions, such as nitrogen reduction,[8,9] carbon dioxide reduction,[10,11] and nitrate remediation,[12–16] remains hindered by the persistent challenge of parasitic side reactions, notably the HER. Conventional strategies, like structural tuning, facet engineering, interfacial modifications, *etc.*,[17–19] have made significant progress, but are often limited by pH dependency, complex fabrication, and reliance on expensive materials.[20,21]

While the effect of electrostatic forces on molecular ordering and self-organization is well known,[22,23] we demonstrate here the electrostatic engineering of surface charges as an adaptive, intelligent gate to regulate reaction fluxes. By imparting static, long-range surface charges to carbon-based electrodes *via* simple, scalable synthesis, we harness electrostatic attraction or repulsion to selectively suppress parasitic pathways, such as the hydrogen evolution reaction (HER), while simultaneously promoting reaction selectivity. This universal, pH-independent strategy transcends traditional material modifications, enabling precise, energy-efficient control over electrochemical selectivity.

To demonstrate this concept, we activate long-range coulombic forces on the electrode surface and demonstrate a substantial suppression of the parasitic HER (Scheme 1), reducing its faradaic contribution by over 35%, while boosting ammonia electrosynthesis by two-fold. Integrating this electrostatic control into an energy-efficient electrochemical reactor reduces the overall energy input by over 50%, establishing that electrostatic decatalysis is a powerful, broadly applicable principle for sustainable electrochemical transformations. This work not only offers a new paradigm for universal, pH-independent catalytic control but also opens avenues to tackle some of the most pressing energy and environmental challenges with fundamental, physics-based strategies rooted in electrostatic modulation.

Influence of the interfacial charge and electrochemical double-layer structure on reaction kinetics is a mature and foundational concept, originating from Frumkin theory[24] and continuing through extensive modern literature[25–27] majorly attributed to microenvironmental wettability and double-layer modulations. We show that irrespective of the surface area, double-layer, and wettability factors electrostatic decatalysis of parasitic reaction leads to distinct catalytic outcomes of reaction selectivity.

Results and discussion

Surface activation of coulombic forces

Carbon nanotubes (CNTs) are widely used in electrochemical devices due to their high electrical conductivity, large surface area, and excellent mechanical and chemical stability. Their nanoscale morphology enables efficient electron transport and abundant active sites, making them an effective support for enhancing catalytic performance. To impart a positive surface

[a]Department of Chemistry, Indian Institute of Science Education and Research, Pune, Dr Homi Bhabha Road, Pune, 411008, India. E-mail: musthafa@iiserpune.ac.in
[b]Department of Chemistry and Biochemistry, University of Texas at Arlington, Texas 76019, USA

Open Access Article. Published on 23 January 2026. Downloaded on 3/17/2026 3:33:40 PM.
This article is licensed under a Creative Commons Attribution-NonCommercial 3.0 Unported Licence.

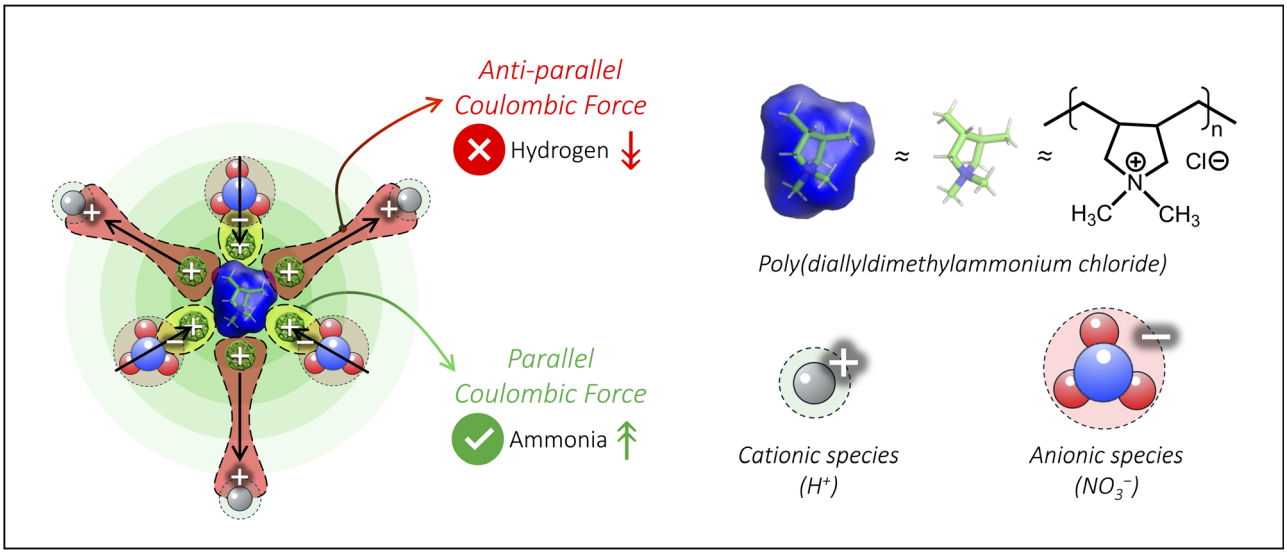

Scheme 1 Illustration of electrostatic decatalysis of parasitic chemistry while selectively favouring the desired reaction flux.

charge on CNTs, we employed poly(diallyldimethylammonium chloride) (PDDA) as a cationic ionomer due to its quaternary ammonium groups. In a typical synthesis, 100 mg CNTs were dispersed in 100 mL of a 5 wt% PDDA solution under sonication for 2 h, followed by stirring for ∼20 h to achieve a homogeneous black suspension. The mixture was then filtered, thoroughly washed to remove excess PDDA, and dried under vacuum for 24 h to obtain the positively charged CNT (p-CNT).[28,29] For negative surface charge engineering, we utilized Nafion ionomer, utilizing its sulphonic acid groups, following the same synthesis protocol, and obtained the n-CNT (Fig. 1a).

Theoretical modeling approaches and molecular dynamics (MD) simulations enable the exploration of atomistic-level details of such modified surfaces, their stability and subsequent spatial effects. Herein, we employed the CHARMM-GUI web tool to model systems involving these complex surface interactions[30] and constructed two surface models using the nanomaterial modeler module[31] of the CHARMM-GUI web platform: one with a positively charged surface (p-CNT model) and one with a negatively charged surface (n-CNT model). Each model represented the CNT surface as a planar graphene patch measuring 54.3 Å × 51.3 Å in the *X*–*Y* plane. This planar representation effectively approximates a local region of a CNT, which typically has outer diameters exceeding 6 nm. At this scale, the curvature is negligible, enabling the planar patch to capture the essential atomic-level features of surface–polymer interactions. Positive and negative surface charge modifications were introduced using the pentameric forms of PDDA and Nafion, respectively (Fig. S1, SI). For each functionalized surface, two independent solvated systems were generated. Each system contained over 26 000 atoms, making a complete quantum mechanical theory treatment computationally prohibitive. Accordingly, we employed a reliable and inexpensive parameterized classical force field level of theory for energy calculations and MD simulations. All simulations were performed using the CHARMM program (c50a1 development version),[32] coupled with the OpenMM engine (version 8.1)[33] for GPU acceleration. Full details of the computational modeling, force field parameterization, and simulation protocols are provided in the SI. To assess the stability of polymer adsorption on CNT surfaces, we then calculated the interaction energies between the graphene patch and the pentamer ionomers from the modeled systems. Averaged over the MD simulation trajectories, the interaction energy was -53.8 ± 0.7 kcal mol^{-1} for the p-CNT model and -47.2 ± 1.1 kcal mol^{-1} for the n-CNT model, indicating thermodynamically favorable adsorption in both cases (Fig. 1b).

Surface engineering was comprehensively characterized using multiple spectroscopic techniques. Attenuated Total Reflectance Infrared (ATR-IR) spectroscopy confirmed the successful surface modification of CNTs through distinct vibrational signatures, as shown in Fig. 1c. The PDDA-functionalized CNTs exhibited characteristic absorption bands at 3356 cm^{-1} (NR_3^+ symmetric stretching), 3000–2800 cm^{-1} (aliphatic C–H stretching), 1645 cm^{-1} (N–C deformation), 1460 cm^{-1} (CH_2 bending), and 1129 cm^{-1} (C–N stretching vibration).[34,35] Similarly, Nafion-modified CNTs displayed signature peaks at 1140 cm^{-1} (CF_2 symmetric stretching), 1050 cm^{-1} (SO_3^- symmetric vibration), and 975 cm^{-1} (C–O–C ether linkage), confirming the presence of the anionic polymer.[36] These well-resolved vibrational features demonstrate the effective incorporation of cationic (PDDA) and anionic (Nafion) modifiers onto the CNT surfaces. In Fig. 1d, Raman spectroscopy reveals significant changes due to surface charge modification through the I_D/I_G (disordered carbon/graphitic peak, 1290/1600 cm^{-1}) ratio analysis, where the increased ratio for both p-CNT (2.39) and n-CNT (2.52) compared to bare-CNT (1.61) indicates higher defect density due to polymer functionalization.[37] Thermal Gravimetric Analysis (TGA) results provided in Fig. 1e give further confirmation through distinct weight loss profiles that correlate with the decomposition temperatures of pure PDDA (∼30–150 °C: water loss; ∼200–350

 © 2026 The Author(s). Published by the Royal Society of Chemistry

Open Access Article. Published on 23 January 2026. Downloaded on 3/17/2026 3:33:40 PM.
This article is licensed under a Creative Commons Attribution-NonCommercial 3.0 Unported Licence.

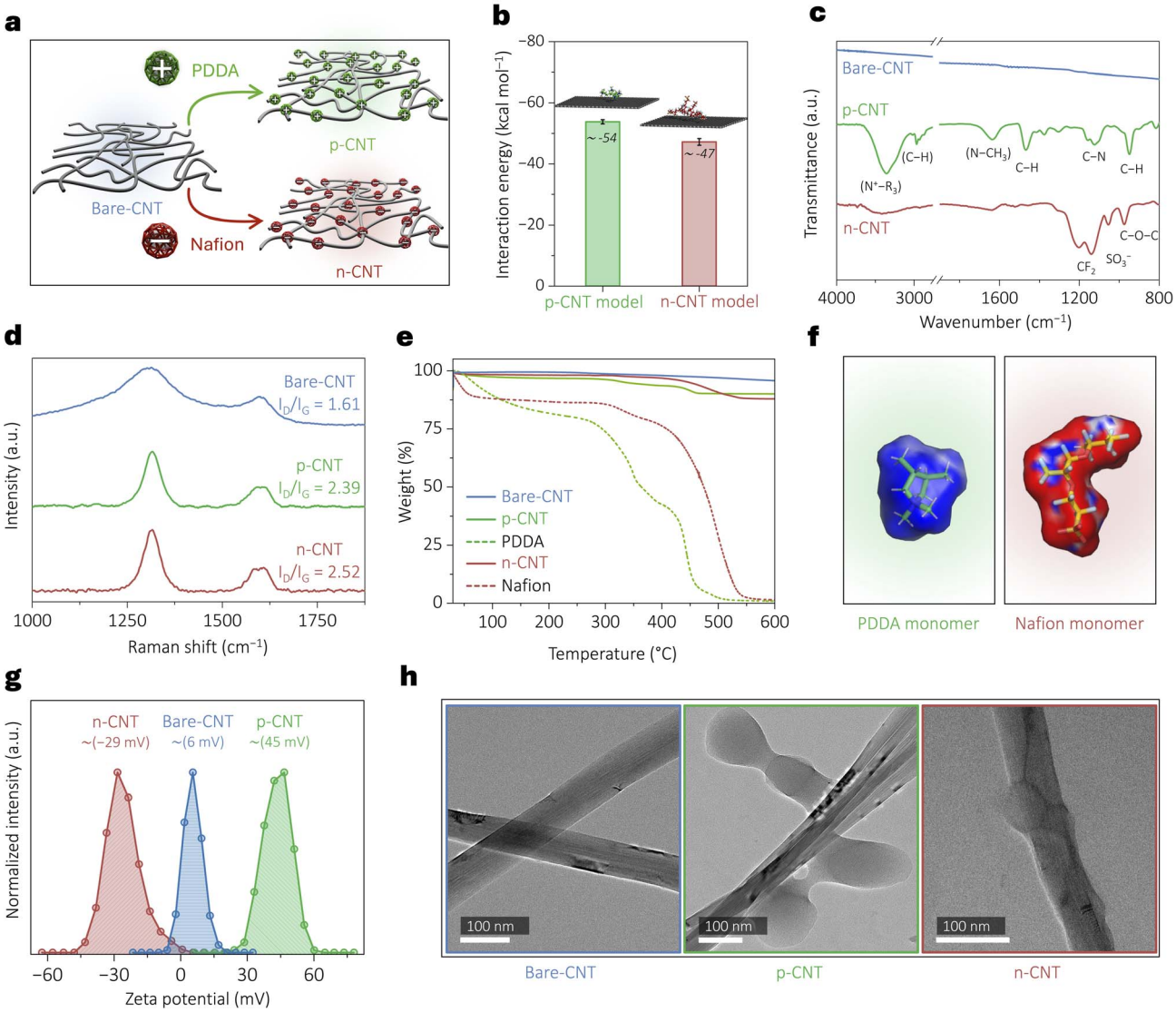

Fig. 1 (a) Illustrative representation of surface charge engineering of CNTs with PDDA as the positive ionomer (p-CNT) and Nafion as the negative ionomer (n-CNT). (b) Theoretical interaction energy of CNTs with ionomers (p-CNT model and n-CNT model). (c) ATR-FTIR spectra, (d) Raman spectra, and (e) TGA curves of modified and unmodified CNTs. (f) Electrostatic surface potential of ionomers. (g) Zeta potential analysis and (h) TEM images of bare-CNT, p-CNT, and n-CNT.

°C: decomposition of quaternary ammonium group; >350 °C: backbone degradation)[38] and Nafion (~30–150 °C: water loss; ~250–400 °C: decomposition of sulfonic acid side chains; >400 °C: backbone degradation),[39] respectively.

We then characterized the electrostatic influence of such charged ionomers that could affect the spatial environment. Poisson–Boltzmann (PB) calculations[40] were performed on the modeled monomeric forms of PDDA and Nafion using the PBEQ module in the CHARMM program. These calculations were conducted using a solute dielectric constant of 1.0, a solvent dielectric constant of 80.0, and an ionic strength of 0.1 M on a special grid of 0.5 Å surrounding the ionomers, matching the aqueous solvent conditions used in the MD simulations (SI). The resulting electrostatic potentials were projected onto the solvent-accessible surface area (SASA) of each molecule to generate spatially interpretable electrostatic maps. As shown in Fig. 1f, the PDDA monomer produced a net positive potential (blue), while the Nafion monomer exhibited a net negative potential (red). These maps qualitatively indicate that the charged ionomers can attract or repel ions (say NO_3^-) through long-range electrostatic interactions. Consistent with these predictions, the zeta potential measurement in Fig. 1g shows values close to +45 mV for p-CNT and −29 mV for n-CNT. As shown in Fig. 1h, morphological examination *via* transmission electron microscopy (TEM) clearly visualized the polymer coatings on CNT surfaces, while high-resolution TEM and X-ray diffraction confirmed that the functionalization process preserved the fundamental structure of the CNTs, as indicated by the maintained (002) plane spacing of 0.33 nm and almost unchanged diffraction patterns (Fig. S2, SI).[41,42] This approach, combining surface-sensitive vibrational spectroscopy, defect analysis, thermal decomposition profiling, surface charge

Open Access Article. Published on 23 January 2026. Downloaded on 3/17/2026 3:33:40 PM.
This article is licensed under a Creative Commons Attribution-NonCommercial 3.0 Unported Licence.

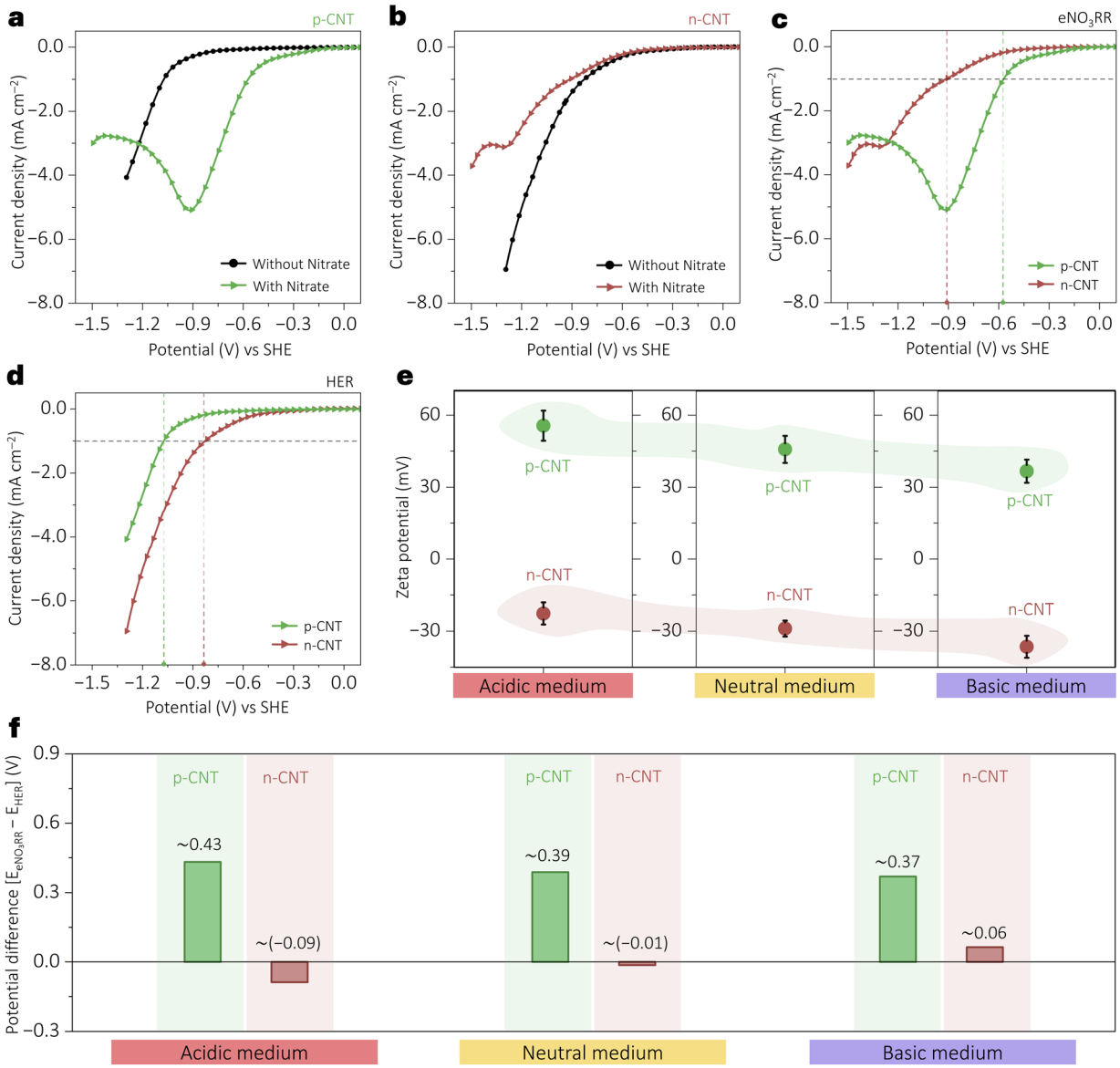

Fig. 2 Linear sweep voltammograms (LSVs) of the HER (without nitrate) and eNO$_3$RR (with nitrate) on (a) p-CNT and (b) n-CNT electrodes in 10 mM $HClO_4$ solution and 10 mM KNO_3 + 10 mM $HClO_4$ solution at a scan rate of 20 mV s^{-1}. (c) Comparison of LSVs for the eNO$_3$RR for p-CNT and n-CNT. (d) Comparison of LSVs for the HER (without nitrate) for pCNT and n-CNT electrodes. (e) Zeta potentials for p-CNT and n-CNTs in acidic, neutral and basic media. (f) Difference between the potentials to achieve a current density of 1 mA cm^{-2} in all the media with nitrate (eNO$_3$RR) and without nitrate (HER) [extracted from Fig. S3, SI].

measurement, and nanoscale imaging, provided unambiguous evidence for the successful surface charge engineering of CNTs with both cationic and anionic surface functionalities while maintaining their structural integrity.

Electrochemical nitrate reduction

These modified electrodes demonstrate the electrostatic decatalysis of the parasitic parallel HER during the electrochemical nitrate reduction reaction (eNO$_3$RR). The electrocatalytic activity of p-CNT (Fig. 2a) and n-CNT (Fig. 2b) toward the eNO$_3$RR was evaluated at room temperature using a three-electrode, single-compartment system *via* linear sweep voltammetry (LSV) in Ar-purged 10 mM $HClO_4$, both with and without 10 mM NO_3^-. Each electrocatalyst was drop-cast onto a glassy carbon (GC) electrode and pre-conditioned by cyclic voltammetry (CV) until a steady-state response was achieved. In Fig. 2c, LSV results show that p-CNT exhibits enhanced eNO$_3$RR activity, reaching a current density of 1 mA cm^{-2} at a lower potential (−0.57 V) compared to n-CNT (−0.91 V), attributed to electrostatic attraction between the positively charged surface (from PDDA functionalization) and the negatively charged NO_3^- ions. In contrast, n-CNT shows suppressed eNO$_3$RR activity, consistent with electrostatic repulsion between the negatively charged sulfonate surface and NO_3^- ions.

Interestingly, in the absence of NO_3^-, LSV (only for the HER) reveals that n-CNT outperforms p-CNT, requiring the lowest

 © 2026 The Author(s). Published by the Royal Society of Chemistry

Open Access Article. Published on 23 January 2026. Downloaded on 3/17/2026 3:33:40 PM.
This article is licensed under a Creative Commons Attribution-NonCommercial 3.0 Unported Licence.

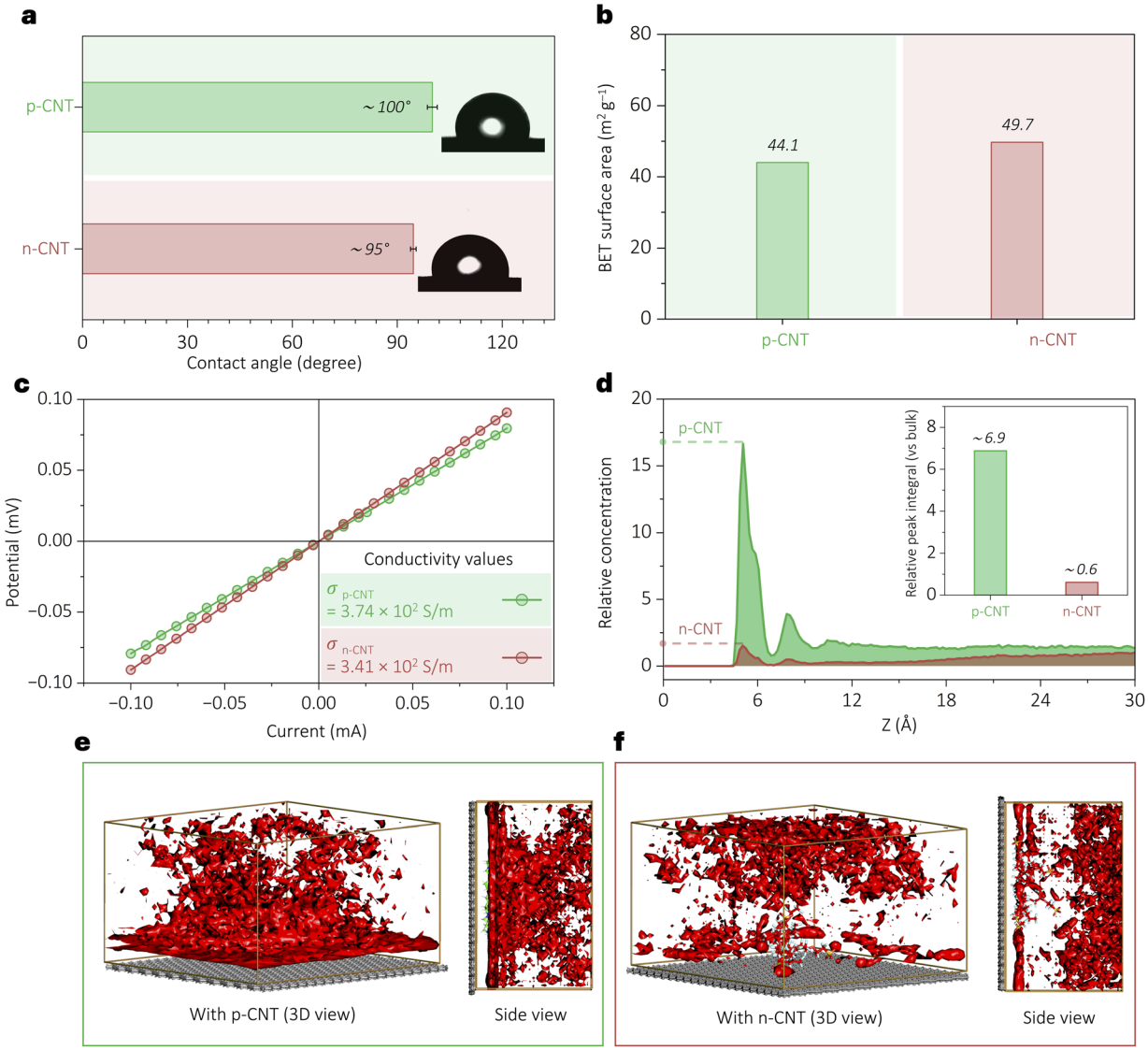

Fig. 3 (a) Hydrophilicity measurement, (b) BET surface area analysis, and (c) I–V plots. (d) NO_3^- ion concentration profile along the Z-axis, perpendicular to the modeled surface, showing deviations from the bulk concentration (0.1 M) to highlight near-surface accumulation or depletion. The inset panel reports the NO_3^- enrichment factor, obtained by integrating the first interfacial peak relative to a flat bulk profile [Fig. S7, SI]. (e and f) Solvation maps of NO_3^- ions near the (e) p-CNT model and (f) n-CNT model surfaces, derived from the corresponding MD simulation trajectories as detailed in the SI.

overpotential to reach 1 mA cm^{-2}, as shown in Fig. 2d. This trend is reversed from that seen in the eNO_3RR (Fig. 2c) and is explained by favorable electrostatic attraction between H^+ and the negatively charged n-CNT surface. Conversely, p-CNT repels protons, requiring a higher potential for the HER, confirming the key role of surface charge in modulating electrocatalytic selectivity. This demonstrates that surface charge-induced electrostatic fields can deactivate or activate parasitic HER pathways depending on their polarity, effectively functioning as a regulator of parasitic reaction flux.

These surface charges are pH independent, and to demonstrate this, zeta potential measurements (Fig. 2e) were conducted at various pH. The results show that p-CNT exhibits a consistent positive zeta potential due to PDDA's pH-independent quaternary ammonium groups, while n-CNT, functionalized with Nafion (which carries a sulfonate group), shows a consistently negative zeta potential. These trends were preserved across acidic, neutral, and basic media, validating the stability of the engineered surface charges. Subsequent eNO_3RR and HER evaluations under neutral and basic conditions (Fig. S3, SI) underline the acidic media trends; p-CNT consistently exhibits superior eNO_3RR performance due to electrostatic attraction between p-CNT and NO_3^-, and consequently the dominance of NO_3^-, while unfavorable for the parasitic HER performance due to electrostatic repulsion between p-CNT and H^+/H_3O^+. The potential difference to achieve 1 mA cm^{-2} current density with nitrate and without nitrate ($\Delta E = E_{eNO3RR} - E_{HER}$) was extracted as a metric for selectivity (Fig. 2f). A larger

Open Access Article. Published on 23 January 2026. Downloaded on 3/17/2026 3:33:40 PM. This article is licensed under a Creative Commons Attribution-NonCommercial 3.0 Unported Licence.

ΔE indicates enhanced eNO_3RR selectivity with minimized HER interference, and p-CNT consistently showed the highest ΔE across all pH conditions.

This study highlights the ability of p-CNT to mitigate the parasitic HER, a major challenge in the eNO_3RR, through electrostatic surface charge control. From the observed performance (Fig. 2), it could be argued that it originates from several surface-modified properties rather than electrostatic effects alone, including wettability changes, accessible surface area variations, or altered electrical properties. To systematically study these possibilities, we conducted various characterization experiments: contact angle measurements (Fig. 3a) revealed a wettability trend (p-CNT: ~100.2°; n-CNT: ~94.6°), which is comparable, suggesting wettability is not the dominant factor. In Fig. 3b, BET surface area analysis showed p-CNT with an area of 44.1 $m^2\ g^{-1}$ and n-CNT with an area of 49.7 $m^2\ g^{-1}$, demonstrating that the enhanced electrochemical activities occur despite the reduced surface area in p-CNT. Fig. 3c shows electrical transport measurements *via* a current–potential (*I–V*) plot (p-CNT: 3.74×10^2 S m^{-1}; n-CNT: 3.41×10^2 S m^{-1}), and the electronic conductivities fall in a similar range. Yet, the p-CNT showed superior eNO_3RR. Electrochemical active surface area (ECSA) assessment through double-layer capacitance measurements (Fig. S4–S6, SI) further confirmed that activity trends (n-CNT > p-CNT) oppose surface area variations. This comprehensive exclusion of wettability (contact angles), electrical conductivity (*I–V* curves), and surface area (BET and ECSA) effects provide substantial evidence that the eNO_3RR and HER performance in Fig. 2 originates primarily from electrostatic interactions within the reaction zone.

MD simulations of solvated surface models revealed how the coulombic force modulates long-range electrostatic effects on NO_3^- local concentration near the electrode surface. The relative concentration profiles show a pronounced accumulation of NO_3^- near the p-CNT surface, whereas the n-CNT surface exhibits a marked depletion (Fig. 3d; details of the analysis are provided in section S2, SI). Analysis of the relative concentration profiles revealed that the NO_3^- concentration was enriched by ~sevenfold near the p-CNT surface, whereas it was reduced to about half near the n-CNT surface, as quantified by the NO_3^- enrichment factor, which measures the integrated intensity of the first interfacial peak relative to the bulk (Fig. 3d inset and S7, SI). These trends were corroborated by solvation maps, which showed enhanced NO_3^- density near the positively charged surface and depletion near the negatively charged surface (Fig. 3e and f). These results demonstrate that coulombic force can be strategically harnessed to tune the local concentration at the interface, thereby enabling control over local ion distributions and, in turn, influencing interfacial reaction kinetics and electrochemical selectivity. Moreover, this approach aims to tackle a key challenge in nitrate reduction: under reducing potentials, the electrode surface acquires a negative charge, which tends to repel the negatively charged nitrate ions and consequently lowers their local concentration near the interface. A nearly sevenfold increase in the NO_3^- enrichment factor (inset of Fig. 3d) suggests that this limitation can be overcome even under negative reduction potentials, by activating coulombic forces at the interface.

Device performance

After successfully verifying the electrostatic interaction in eNO_3RR studies, we have integrated this approach into a practical two-electrode ammonia synthesizer. To enable this in an energy-efficient way, firstly, systematic voltammetric screening (Fig. 4a and Table S1) was attempted to replace the sluggish counter electrode oxygen evolution reaction (OER) by a potential oxidation reaction. To achieve this, various species, including iron complexes, ruthenium complexes, ferrocene derivatives, TEMPO radicals, viologens, and quinone derivatives, were screened. From the analyses, ferrocyanide emerged as the superior choice due to its cost efficiency ($0.14 per gram; Sigma-Aldrich), which is remarkably low compared to the rest of the species, as shown in Fig. 4b. Cyclic voltammetric studies using platinum, gold, and glassy carbon electrodes (Fig. 4c) confirmed the reaction's electrode-independent nature, allowing the use of low-cost carbon electrodes to drive the reaction instead of precious metals. At sufficiently positive potentials, the redox behaviour of ferrocyanide (FOR) is mass transport-limited, with a near 0.5 slope in log (*i*) *vs.* log (*v*) plots (Fig. S8a–c, SI) and a diffusion coefficient (*D*) of $\sim 3.7 \times 10^{-6}$ $cm^2\ s^{-1}$ (calculation S1, SI).[43] Rotating disk electrode (RDE) studies further confirm a single-electron transfer process ($n \approx 1$ from Levich analysis; Fig. S8d and e, calculation S2, SI) and a concentration-dependent current response (Fig. S8f, SI), supporting FOR's electrochemical suitability. Notably, the FOR requires ~1.2 V lower potential than the conventional oxygen evolution reaction (OER), as shown in three-electrode measurements (Fig. S9, SI).

After analysing this behaviour, we fabricated the ammonia electrosynthesizer by coupling the eNO_3RR (on p-CNT and n-CNT driving electrodes) with the FOR system (on a bare carbon electrode). Compared to the conventional eNO_3RR‖OER setup, the eNO_3RR‖FOR configuration with n-CNT showed a ~1.3 V less potential to reach 50 mA cm^{-2} (Fig. 4d). The input potential is further reduced for p-CNT due to the incorporation of the electrostatic effect. The sustained low-voltage operation was confirmed further *via* chronopotentiometry (Fig. 4e). When p-CNT was employed as the eNO_3RR electrocatalyst, the operating potential decreased further, resulting in an overall reduction of approximately 1.7 V compared to the conventional eNO_3RR‖OER configuration. Collectively, employing the FOR as the anodic reaction and p-CNT as the driving electrode in device-level ammonia synthesis offers significant energy savings and cost advantages.

To confirm ammonia formation in the cathodic compartment of the eNO_3RR‖FOR systems, a preliminary qualitative test was performed using Nessler's reagent.[44] The appearance of a yellow-brown coloration (Fig. 5a) in the catholyte after electrolysis (absent prior to the reaction) indicates the presence of NH_3 *via* the formation of the iodide complex of Millon's base [$HgO \cdot Hg(NH_2)I$]. To further validate the origin of ammonia from nitrate and eliminate contributions from external nitrogen sources (*e.g.*, N_2), isotope-labeling experiments were conducted using a $K^{15}NO_3$ electrolyte. The post-electrolysis ^1H NMR spectra (Fig. 5b) exhibited distinct doublet peaks for $^{15}NH_4^+$ ($J = 73$ Hz) and a triplet for $^{15}NH_4^+$ ($J = 52$ Hz), while no such signals

 © 2026 The Author(s). Published by the Royal Society of Chemistry

Open Access Article. Published on 23 January 2026. Downloaded on 3/17/2026 3:33:40 PM.
This article is licensed under a Creative Commons Attribution-NonCommercial 3.0 Unported Licence.

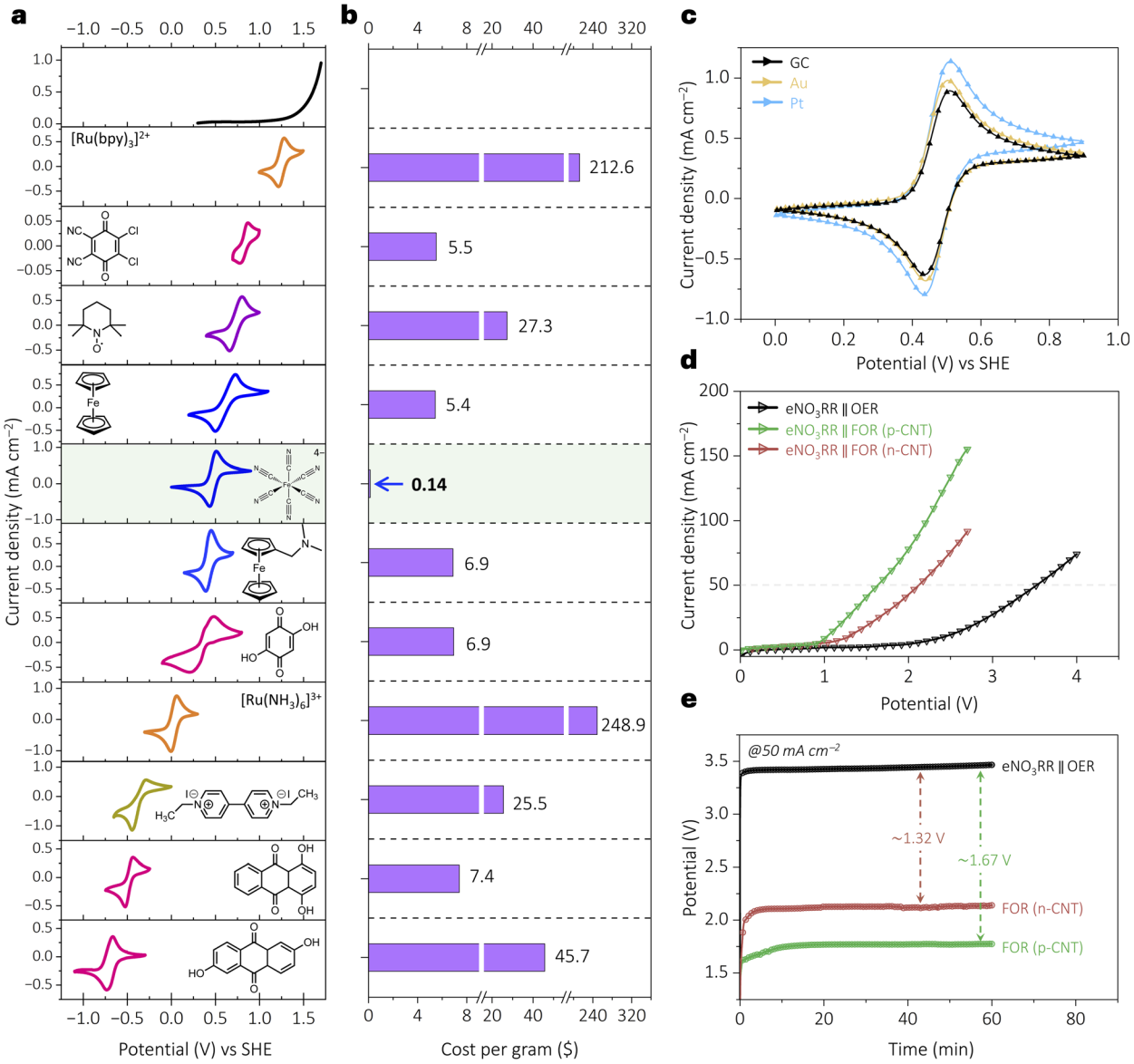

Fig. 4 (a) Cyclic voltammetry of candidate anolytes (including iron complexes, ruthenium complexes, ferrocene derivatives, TEMPO radicals, viologens and quinone derivatives) measured at 20 mV s^{-1} and 10 mM active species concentration. (b) Cost comparisons of the redox species (data sourced from Sigma-Aldrich, India). (c) Electrochemical behavior of ferrocyanide on Pt, Au, and GC electrodes. (d) Polarization curves for the electrochemical nitrate reduction reaction (eNO_3RR) when the counter-reaction is the ferrocyanide oxidation reaction (FOR) instead of the OER. The eNO_3RR was carried out on p-CNT and n-CNT driving electrodes to compare their device level performance. (e) Corresponding chronopotentiometry profiles at 50 mA cm^{-2} when the OER was replaced by the FOR.

were present in the pre-electrolysis solution.[45] These results confirm that NO_3^- is the exclusive nitrogen source for NH_3 production in this system. In Fig. 5c, hydrogen evolution in the cathodic half-cell was verified for all electrodes using *in situ* electrochemical mass spectrometry by monitoring the $m/z = 2$ signal during electrolysis at 50 mA cm^{-2}. Notably, the noticeably lower H_2 partial pressure with the p-CNT electrode at the same current density indicates that coulombic interactions exert deliberate, site- and flux-selective modulation of parasitic pathways. As protons are positively charged, electrodes with static positive surface charge (such as p-CNT) electrostatically repel them, effectively suppressing the parasitic HER.

Given the complexity of the multi-electron NO_3^- to NH_4^+ reduction, side-product formation was investigated using *in situ* electrochemical mass spectrometry and UV-vis spectroscopy. Negligible formation of typical byproducts, such as nitrogen (N_2), nitric oxide (NO), nitroxyl (HNO), nitrous oxide (N_2O), and nitrogen dioxide gas (NO_2), hydrazine (NH_2–NH_2), and hydroxylamine (NH_2OH) were observed (Fig. S10–S12, SI). However, we observed nitrite (NO_2^-) as a major by-product during the electrolysis (FE for p-CNT ~19% and for n-CNT ~33%) (Fig. S13 and S14, SI). Its quantification was carried out by UV-vis spectroscopic analysis with the help of calibration plots (Fig. S13, calculation S3, SI) constructed using standard known

Open Access Article. Published on 23 January 2026. Downloaded on 3/17/2026 3:33:40 PM.
This article is licensed under a Creative Commons Attribution-NonCommercial 3.0 Unported Licence.

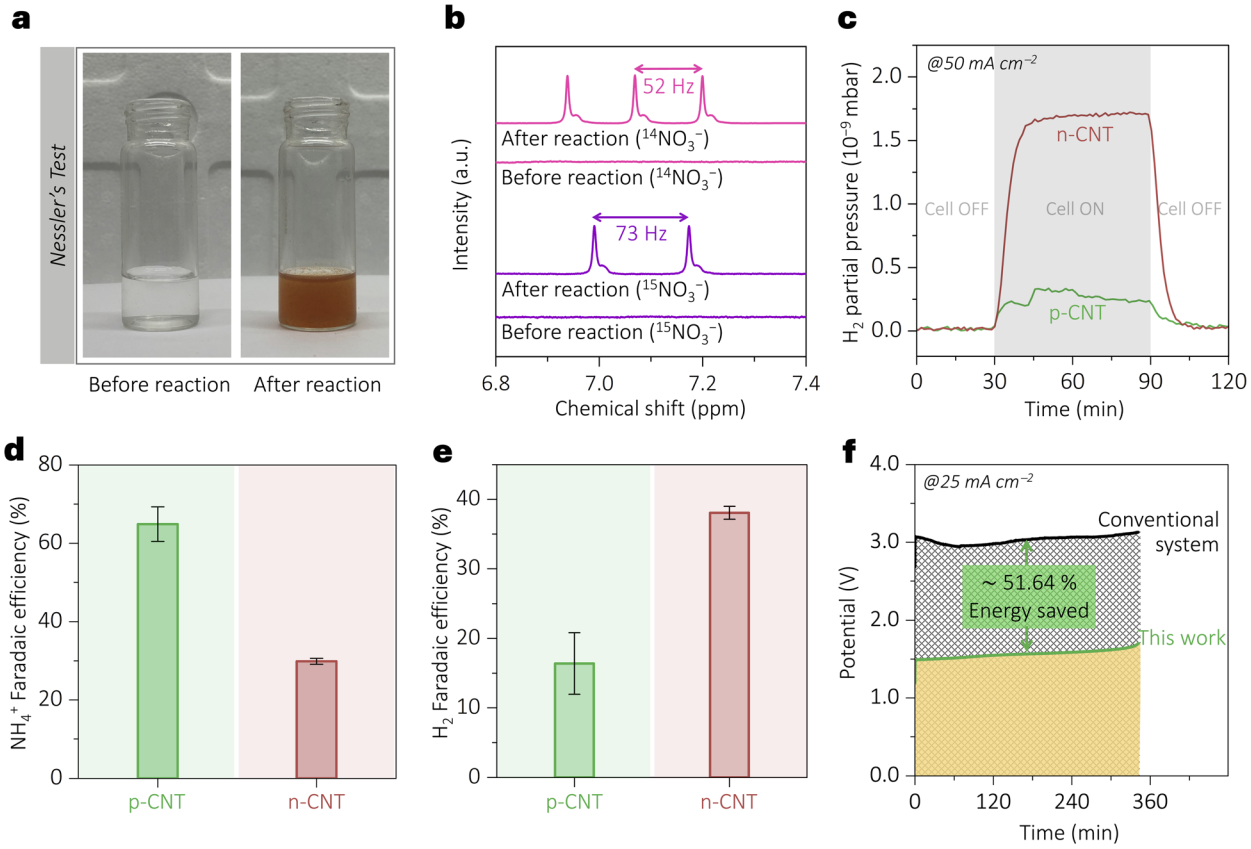

Fig. 5 (a) Nessler's reagent test for ammonia detection, before and after electrolysis. The characteristic yellow-brown colouration of ammonia after electrolysis suggests the conversion of nitrate to ammonia. (b) ^{1}H NMR spectra of the electrolyte before and after the eNO_3RR using $^{15}NO_3^-$ and $^{14}NO_3^-$ as the nitrogen sources. (c) *In-situ* electrochemical mass spectra of the cathodic outlet of the $eNO_3RR||FOR$ at a constant current density of 50 mA cm^{-2}. (d) Faradaic efficiency (FE) of ammonia (NH_4^+) using p-CNT and n-CNT as the driving electrodes. (e) Faradaic efficiency of H_2 with p-CNT and n-CNT electrodes. (f) Total energy savings of the $eNO_3RR||FOR$ (with p-CNT) compared to the conventional electrolyzer system ($eNO_3RR||OER$).

concentrations (as detailed in the Experimental section, SI). The ratio of ammonia formed *vs.* nitrite produced is fairly constant over time for both p-CNT and n-CNT electrodes (Fig. S15, SI). Whether nitrite is a kinetically trapped intermediate or an end product is a matter of future investigation. Ammonia formation was quantified by ^{1}H NMR analysis of the electrolyte after 1 hour of electrolysis at 50 mA cm^{-2} (Fig. 4e), using calibration curves constructed from standard ammonia solutions (Fig. S16, SI). The faradaic efficiency (FE) of ammonia was nearly ~65% on p-CNT and ~30% on n-CNT electrodes (Fig. 5d, calculation S4, SI). Notably, p-CNT exhibited more than twofold enhancement in the FE over n-CNT (Fig. 5d, calculation S5, SI), attributed to favorable electrostatic interactions. These results validate the viability of our approach in a two-compartment device system. Since no major side products could be detected other than nitrite, the FE of H_2 evolution was calculated from FEs of ammonia and nitrite, as shown in Fig. 5e (calculation S6, SI).

These results demonstrate that p-CNT, as a cathodic electrocatalyst, selectively enhances NO_3^- reduction (Fig. 5d) to ammonia while suppressing the parasitic HER (Fig. 5e). The inverse trends observed in the FE of NH_4^+ and H_2 are attributed to its static electrostatic effect, which favors NO_3^- attraction toward the positively charged p-CNT while simultaneously repelling H^+ ions. Energy analysis (Fig. 5f, calculation S7, SI) reveals that combining the eNO_3RR with the FOR (eNO_3-$RR||FOR$) with electrostatic charge modulation (p-CNT as the electrocatalyst) achieves 125.209 kJ mol^{-1} (~50%) energy reduction compared to the conventional system (eNO_3-$RR||OER$), highlighting the dual advantages of electrostatic decatalysis in this system.

To evaluate the stability of the p-CNT electrode, the device was operated in a wide current density range (10 to 100 mA cm^{-2} and back to 10 mA cm^{-2}). As shown in Fig. 6a, the system maintained consistent electrochemical activity. Durability was further validated through long term chronopotentiometry at a fixed current density of 10 mA cm^{-2} for ~30 hours (Fig. S17, SI) and rate capability tests (Fig. 6b), with ammonia quantified at each step. The faradaic efficiency remained nearly constant across all current densities (Fig. 6c, S18 and SI), confirming the stability of p-CNT under practically relevant conditions. To probe the suppression of the competing hydrogen evolution reaction (HER), H_2 partial pressures were monitored during electrolysis at low and high current densities. p-CNT consistently exhibited suppressed HER in the full current range (Fig. 6d and e, S19, SI), attributed to the dominance of NO_3^- near the positively charged surface, in contrast to n-CNT.

 © 2026 The Author(s). Published by the Royal Society of Chemistry

Open Access Article. Published on 23 January 2026. Downloaded on 3/17/2026 3:33:40 PM.
This article is licensed under a Creative Commons Attribution-NonCommercial 3.0 Unported Licence.

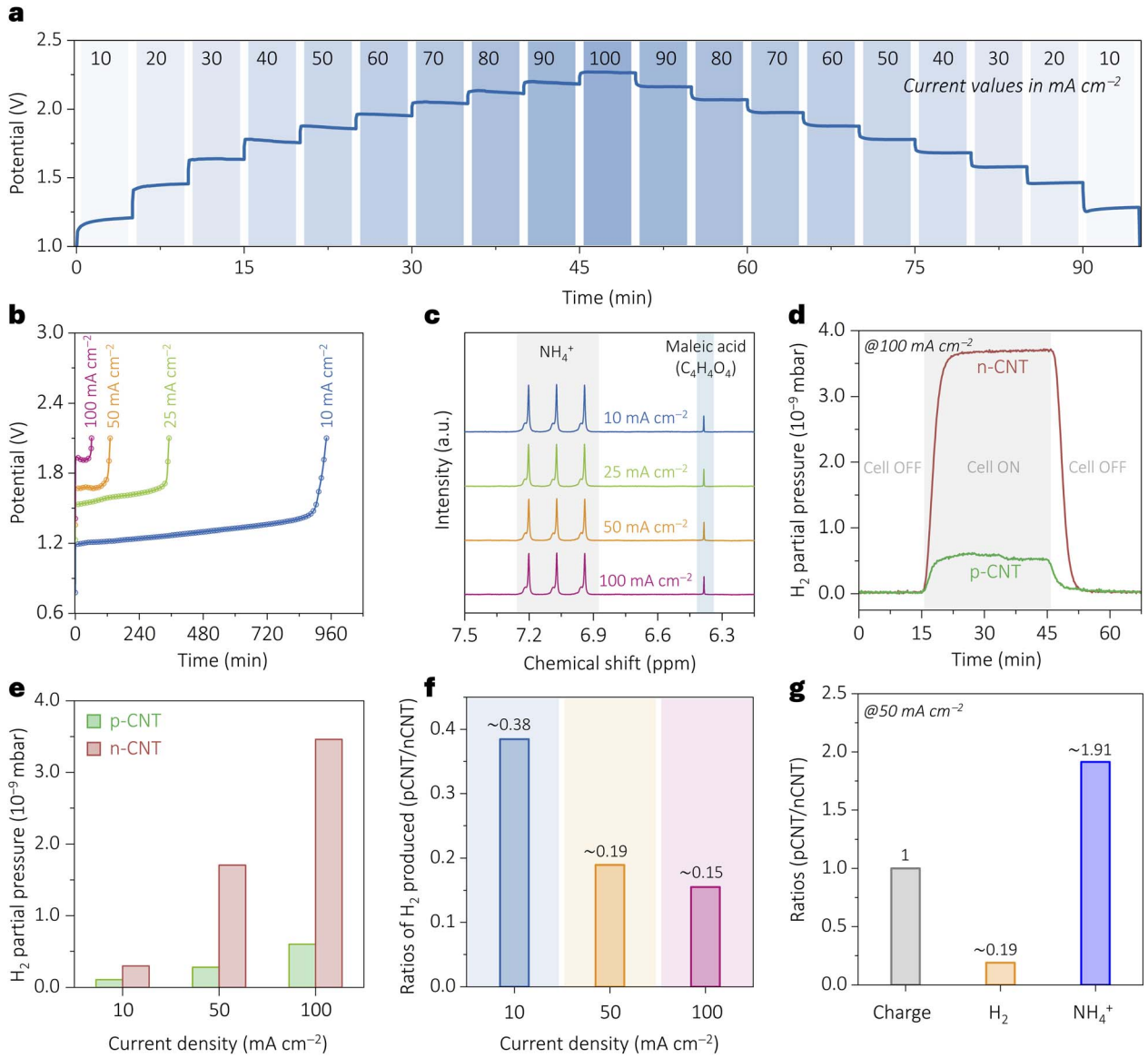

Fig. 6 (a) Stair-case stability test at various current densities (10 mA cm^{-2} to 100 mA cm^{-2}) for the $eNO_3RR||FOR$ cell with p-CNT as the driving electrode for the eNO_3RR. (b) Rate capability study of the $eNO_3RR||FOR$ cell with the p-CNT electrode. (c) ^1H NMR spectra of the electrolyte after electrolysis at various current densities. (d) Electrochemical mass spectra at a high current density of 100 mA cm^{-2} (e) H_2 production on p-CNT *vs.* n-CNT at various current densities. (f) Ratios of H_2 produced on p-CNT *vs.* n-CNT at different current densities. (g) Ratios of charge, H_2 produced, and ammonia synthesized on p-CNT *vs.* n-CNT at 50 mA cm^{-2}.

Although the HER is typically increasingly favored at higher current densities, it displays diametrically opposite trends on p-CNT *vs.* n-CNT electrodes (Fig. 6e).

Electrochemical mass spectrometry reveals that the H_2 partial pressure increases only modestly on p-CNT, whereas it rises sharply on n-CNT (Fig. 6e). Consequently, the ratio of H_2 produced on p-CNT relative to n-CNT decreases markedly with increasing current density, indicating that a substantially larger fraction of the applied charge is directed toward nitrate-to-ammonia conversion on p-CNT electrodes (Fig. 6f). At 50 mA cm^{-2}, this selectivity manifests as a pronounced divergence between H_2 production (~0.2) and ammonia synthesis (~1.9) on p-CNT relative to n-CNT for the same charge input (Fig. 6g).

As variations in wettability, electronic conductivity and surface area have been ruled out, these results confirm that electrostatic effects not only modulate reaction kinetics through additional electrostatic currents but also decatalyze parasitic pathways, thereby actively governing catalytic outcomes and selectivity under technologically relevant conditions. Post-experimental characterization techniques (zeta potential measurement, SEM, TEM, ATR-IR, and XRD) confirm the structural integrity of the p-CNT electrode. In Fig. S20 (ESI), zeta potential shows a minimal change after the eNO_3RR. In Fig. S21 and S22 (ESI), SEM and TEM images revealed a stable PDDA layer anchored to the functionalized CNTs, while ATR-IR and XRD confirmed its chemical stability (Fig. S23 and S24, SI).

Open Access Article. Published on 23 January 2026. Downloaded on 3/17/2026 3:33:40 PM.
This article is licensed under a Creative Commons Attribution-NonCommercial 3.0 Unported Licence.

These results affirm that PDDA remains robustly attached to the p-CNT surface, contributing to sustained performance.

Conclusions

We enhance electrochemical performance by enabling electrostatic decatalysis of competing reaction pathways, thereby redefining catalytic selectivity. In contrast to conventional catalyst design strategies that are often constrained by pH and surface chemistry, electrostatic decatalysis provides a scalable, adaptive, and pH-independent route for reaction control. Through deliberate engineering of interfacial charge distributions, the parasitic hydrogen evolution reaction is effectively suppressed, while nitrate-to-ammonia conversion is selectively promoted by nearly twofold, resulting in over ∼50% energy savings at the device level. These results establish electrostatic decatalysis as a viable strategy for steering selectivity in sustainable electrochemical transformations.

Author contributions

B. N. performed all the experiments and analyzed the data with H. P. and R. M. A. A. T. performed the theoretical modeling, simulations, and trajectory analysis. M. O. T. conceptualized and supervised the work. The manuscript was finalized with input from all the authors.

Conflicts of interest

There are no conflicts to declare.

Data availability

The data supporting this article have been included as part of the supplementary information (SI). Supplementary information: experimental sections; computational models and methods; supporting figures, calculations and references. See DOI: https://doi.org/10.1039/d5sc08236f.

Acknowledgements

M. O. T. acknowledges financial support from the BITS BioCyTiH foundation BBF/BITS/FY2024-25/ART-304 and DST-WTI (DST/TMD EWO/WTI/2K19/EWFH/2019/272). B. N. thanks the University Grants Commission (UGC), India, for fellowship support. We thank Dr Kwangho Nam (Associate Professor, The University of Texas at Arlington) for helpful discussions on MD simulation strategies. We also acknowledge the IISER Pune for providing access to essential research facilities.

References

1 R. B. Jethwa, S. Mondal, B. Pant and S. A. Freunberger, *Angew. Chem. Int. Ed.*, 2024, **63**, e202316476.
2 L. Abisdris, M. S. Naeem, M. Bianchini, I. Herraiz-Cardona, J. Tzadikov, A. Azoulay, R. Geva, M. Volokh, J. H. Baraban, N. López and M. Shalom, *Adv. Energy Mater.*, 2025, **15**, 2502150.
3 F. Makhlooghiazad, L. Miguel Guerrero Mejía, G. Rollo-Walker, D. Kourati, M. Galceran, F. Chen, M. Deschamps, P. Howlett, L. A. O'Dell and M. Forsyth, *J. Am. Chem. Soc.*, 2024, **146**, 1992–2004.
4 Y. Liang, X. Fan, X. He, D. Zheng, S. Sun, Y. Luo, H. Chen and X. Sun, *Nano Res.*, 2025, **18**, 94907344.
5 Y. Ren, Q. Zhou, J. Li, X. He, X. Fan, Y. Fu, X. Fang, Z. Cai, S. Sun, M. S. Hamdy, J. Zhang, F. Gong, Y. Liu and X. Sun, *J. Colloid Interface Sci.*, 2023, **645**, 806–812.
6 P. J. McHugh, A. D. Stergiou and M. D. Symes, *Adv. Energy Mater.*, 2020, **10**, 2002453.
7 R. S. Sánchez, A. Villanueva-Antolí, A. Bou, M. Ruiz-Murillo, I. Mora-Seró and J. Bisquert, *Adv. Mater.*, 2023, **35**, 2207993.
8 S. Paul, A. Adalder, N. Barman, R. Thapa, A. Bera, K. Mitra and U. K. Ghorai, *Adv. Funct. Mater.*, 2024, **34**, 2408314.
9 S. Zhu, K. Liu, Z. Feng, H. Jiang and J. Lin, *Nano Res. Energy*, 2025, **4**, e9120188.
10 S. S. Lavate and R. Srivastava, *Energy Adv.*, 2024, **3**, 2801–2811.
11 X. Fan, C. Liu, X. He, Z. Li, L. Yue, W. Zhao, J. Li, Y. Wang, T. Li, Y. Luo, D. Zheng, S. Sun, Q. Liu, L. Li, W. Chu, F. Gong, B. Tang, Y. Yao and X. Sun, *Adv. Mater.*, 2024, **36**, 2401221.
12 A. Adalder, S. Paul, N. Barman, A. Bera, S. Sarkar, N. Mukherjee, R. Thapa and U. K. Ghorai, *ACS Catal.*, 2023, **13**, 13516–13527.
13 L. Niu, Y. Wang, H. Yin, T. Wang, H. Guo, H. Xian, X. Sun, X. Guo and T. Li, *Adv. Mater.*, 2025, e17303.
14 Y. Lv, J. Ren, M. Jiang, R. Wang, H. Guo, X. Sun, X. Guo and T. Li, *ACS Catal.*, 2025, **15**, 8094–8102.
15 X. Fan, C. Ma, D. Zhao, Z. Deng, L. Zhang, Y. Wang, Y. Luo, D. Zheng, T. Li, J. Zhang, S. Sun, Q. Lu and X. Sun, *J. Colloid Interface Sci.*, 2023, **630**, 714–720.
16 X. Fan, D. Zhao, Z. Deng, L. Zhang, J. Li, Z. Li, S. Sun, Y. Luo, D. Zheng, Y. Wang, B. Ying, J. Zhang, A. A. Alshehri, Y. Lin, C. Tang, X. Sun and Y. Zheng, *Small*, 2023, **19**, 2208036.
17 G. S. Phun, R. Bhide and S. Ardo, *Energy Environ. Sci.*, 2023, **16**, 4593–4611.
18 A. Bovas and T. P. Radhakrishnan, *ChemCatChem*, 2024, **16**, e202400259.
19 L. Li, Y. Xia, M. Zeng and L. Fu, *Chem. Soc. Rev.*, 2022, **51**, 7327–7343.
20 P. H. van Langevelde, I. Katsounaros and M. T. M. Koper, *Joule*, 2021, **5**, 290–294.
21 M. K. Debe, *Nature*, 2012, **486**, 43–51.
22 K. Cui, I. Dorner and S. F. L. Mertens, *Curr. Opin. Electrochem.*, 2018, **8**, 156–163.
23 K. Cui, O. Ivasenko, K. S. Mali, D. Wu, X. Feng, K. Müllen, S. De Feyter and S. F. L. Mertens, *Chem. Commun.*, 2014, **50**, 10376–10378.
24 A. N. Frumkin, *Trans. Faraday Soc.*, 1959, **55**, 156–167.
25 Y. Liu, Y. Zheng, Y. Ren, Y. Wang, S. You and M. Liu, *Environ. Sci. Technol.*, 2024, **58**, 7228–7236.
26 W. Chen, L.-L. Zhang, Z. Wei, M.-K. Zhang, J. Cai and Y.-X. Chen, *Phys. Chem. Chem. Phys.*, 2023, **25**, 8317–8330.
27 H. Khani, A. R. Puente Santiago and T. He, *Angew. Chem. Int. Ed.*, 2023, **62**, e202306103.

 © 2026 The Author(s). Published by the Royal Society of Chemistry

Open Access Article. Published on 23 January 2026. Downloaded on 3/17/2026 3:33:40 PM.
This article is licensed under a Creative Commons Attribution-NonCommercial 3.0 Unported Licence.

28 D. Q. Yang, J. F. Rochelte and E. Sacher, *J. Phys. Chem. B*, 2005, **109**, 4481–4484.
29 B. Nayak, R. Mondal and M. Ottakam Thotiyl, *Nanoscale*, 2023, **15**, 14468–14475.
30 S. Jo, T. Kim, V. G. Iyer and W. Im, *J. Comput. Chem.*, 2008, **29**, 1859–1865.
31 Y. K. Choi, N. R. Kern, S. Kim, K. Kanhaiya, Y. Afshar, S. H. Jeon, S. Jo, B. R. Brooks, J. Lee, E. B. Tadmor, H. Heinz and W. Im, *J. Chem. Theory Comput.*, 2022, **18**, 479–493.
32 W. Hwang, S. L. Austin, A. Blondel, E. D. Boittier, S. Boresch, M. Buck, J. Buckner, A. Caflisch, H. T. Chang, X. Cheng, Y. K. Choi, J. W. Chu, M. F. Crowley, Q. Cui, A. Damjanovic, Y. Deng, M. Devereux, X. Ding, M. F. Feig, J. Gao, D. R. Glowacki, J. E. Gonzales, M. B. Hamaneh, E. D. Harder, R. L. Hayes, J. Huang, Y. Huang, P. S. Hudson, W. Im, S. M. Islam, W. Jiang, M. R. Jones, S. Käser, F. L. Kearns, N. R. Kern, J. B. Klauda, T. Lazaridis, J. Lee, J. A. Lemkul, X. Liu, Y. Luo, A. D. MacKerell, D. T. Major, M. Meuwly, K. Nam, L. Nilsson, V. Ovchinnikov, E. Paci, S. Park, R. W. Pastor, A. R. Pittman, C. B. Post, S. Prasad, J. Pu, Y. Qi, T. Rathinavelan, D. R. Roe, B. Roux, C. N. Rowley, J. Shen, A. C. Simmonett, A. J. Sodt, K. Töpfer, M. Upadhyay, A. van der Vaart, L. I. Vazquez-Salazar, R. M. Venable, L. C. Warrensford, H. L. Woodcock, Y. Wu, C. L. Brooks, B. R. Brooks and M. Karplus, *J. Phys. Chem. B*, 2024, **128**, 9976–10042.
33 P. Eastman, R. Galvelis, R. P. Peláez, C. R. A. Abreu, S. E. Farr, E. Gallicchio, A. Gorenko, M. M. Henry, F. Hu, J. Huang, A. Krämer, J. Michel, J. A. Mitchell, V. S. Pande, J. P. Rodrigues, J. Rodriguez-Guerra, A. C. Simmonett, S. Singh, J. Swails, P. Turner, Y. Wang, I. Zhang, J. D. Chodera, G. De Fabritiis and T. E. Markland, *J. Phys. Chem. B*, 2024, **128**, 109–116.
34 N. Y. Stozhko, E. I. Khamzina, M. A. Bukharinova, A. V. Tarasov, V. Y. Kolotygina, N. V. Lakiza and E. D. Kuznetcova, *Nanomaterials*, 2022, **12**, 4197.
35 B. Nayak, A. R. Arattu Thodika, H. Kumar, R. Thimmappa and M. Ottakam Thotiyl, *J. Colloid Interface Sci.*, 2024, **662**, 289–297.
36 R. Sigwadi, M. S. Dhlamini, T. Mokrani, F. Ṇemavhola, P. F. Nonjola and P. F. Msomi, *Heliyon*, 2019, **5**, e02240.
37 Y. L. Liu, Y. H. Su, C. M. Chang, Suryani, D. M. Wang and J. Y. Lai, *J. Mater. Chem.*, 2010, **20**, 4409–4416.
38 G. G. Celestino, R. R. Henriques, A. L. Shiguihara, V. R. L. Constantino, R. de Siqueira Melo and J. Amim Júnior, *Environ. Sci. Pollut. Res.*, 2019, **26**, 28444–28454.
39 S. Gahlot, H. Gupta and V. Kulshrestha, *Polym. Bull.*, 2017, **74**, 4437–4452.
40 A. Nicholls and B. Honig, *J. Comput. Chem.*, 1991, **12**, 435–445.
41 Z. Xiang, Z. Hu, D. Cao, W. Yang, J. Lu, B. Han and W. Wang, *Angew. Chem. Int. Ed.*, 2011, **50**, 491–494.
42 M. M. Ngoma, M. Mathaba and K. Moothi, *Sci. Rep.*, 2021, **11**, 23805.
43 A. J. Bard, L. R. Faulkner and H. S. White, in:*Electrochemical methods: fundamentals and applications*, John Wiley & Sons, 2022.
44 Y. Zhao, R. Shi, X. Bian, C. Zhou, Y. Zhao, S. Zhang, F. Wu, G. I. N. Waterhouse, L. Wu, C. Tung and T. Zhang, *Adv. Sci.*, 2019, **6**, 1802109.
45 A. Assafiri, C. Jia, D. S. Thomas, D. B. Hibbert and C. Zhao, *Small Methods*, 2024, **8**, 2301373.